New oscillatory instability of a confined cylinder in a flow below the vortex shedding threshold

B. Semin[1]†, **A. Decoene**[2], **J.-P. Hulin**[1], **M. L. M. François**[1] **and H. Auradou**[1]

[1] Laboratoire FAST, Université Paris-Sud, Université Pierre et Marie Curie–Paris 6, CNRS, Bat. 502, Campus Univ., Orsay, F-91405, France

[2] Department of Mathematics, Université Paris-Sud, Bat. 452, Campus Univ., Orsay, F-91405, France

A new type of flow-induced oscillation is reported for a tethered cylinder confined inside a Hele-Shaw cell (ratio of cylinder diameter to cell aperture, $D/h = 0.66$) with its main axis perpendicular to the flow. This instability is studied numerically and experimentally as a function of the Reynolds number Re and of the density ρ_s of the cylinder. This confinement-induced vibration (CIV) occurs above a critical Reynolds number $Re_c \sim 20$ much lower than for Bénard–Von Kármán vortex shedding behind a fixed cylinder in the same configuration ($Re_{BVK} = 111$). For low ρ_s values, CIV persists up to the highest Re value investigated ($Re = 130$). For denser cylinders, these oscillations end abruptly above a second value of Re larger than Re_c and vortex-induced vibrations (VIV) of lower amplitude appear for $Re \sim Re_{BVK}$. Close to the first threshold Re_c, the oscillation amplitude variation as $(Re - Re_c)^{1/2}$ and the lack of hysteresis demonstrate that the process is a supercritical Hopf bifurcation. Using forced oscillations, the transverse position of the cylinder is shown to satisfy a Van der Pol equation. The physical meaning of the stiffness, amplification and total mass coefficients of this equation are discussed from the variations of the pressure field.

Key words: flow–structure interactions, instability, low-dimensional models

1. Introduction

Flow-induced oscillations of slender structures facing a flow are of interest in many domains of engineering, such as the design of tubular structures of offshore platforms, heat exchangers or chemical reactors (see e.g. Sarpkaya 2004; Williamson & Govardhan 2004). Most previous experimental and numerical fundamental studies often considered a rigid circular cylinder transverse to a fluid flow with no lateral confinement and with only one degree of freedom perpendicular to both the flow and to the axis of the cylinder (see e.g. Anagnostopoulos & Bearman 1992; Gabbai & Benaroya 2005; Williamson & Govardhan 2008).

The present work deals, in contrast, with a tethered cylinder strongly confined between two parallel plane walls: the confinement is characterized by the ratio between the cylinder diameter $\bar{D}$ and the cell aperture $\bar{h}$ which is equal to 0.66. This configuration corresponds to important recent applications at lower Reynolds numbers,

† Email address for correspondence: semin@fast.u-psud.fr

such as the enhancement of mixing or heat exchange in microfluidic circuits (see Meis *et al.* 2010) or the design of energy-harvesting devices on a chip (Sánchez-Sanz, Fernandez & Velazquez 2009). It will be shown that, when the cylinder is sufficiently confined, it oscillates spontaneously above $Re \sim 20$ (where the Reynolds number Re is defined using the mean velocity and the aperture $\bar{h}$). This value is well below the threshold for Bénard–Von Kármán vortex shedding ($Re_{BVK} = 111$ for this particular geometry). This result and the variation of the characteristics of the oscillations with the control parameters imply that these oscillations – referred to in the following as confinement-induced vibrations (CIV) – strongly differ from the vortex-induced vibrations (VIV) studied by previous investigators. The latter usually considered dense cylinders constrained elastically: their transverse position satisfies a forced damped harmonic oscillator equation in which the driving force term is associated with the fluctuating lift induced by vortex shedding.

Other recent studies have investigated related effects either at Reynolds numbers below the vortex shedding threshold or for structures without a natural frequency. In the first case, oscillations have been predicted numerically by Cossu & Morino (2000) and Mittal & Singh (2005), but only if an external elastic restoring force is present. In the second, Shiels, Leonard & Roshko (2001) considered a massless cylinder with no restoring force: however, the Reynolds number was higher than here (100) so that vortex shedding took place. Still, at high Reynolds numbers and with no restoring force, experiments by Govardhan & Williamson (2002) demonstrated that large-amplitude vibrations occur below a critical value of the mass; the same observation was made by Horowitz & Williamson (2006) on transverse motions of the trajectory of light cylinders rising in a stationary fluid.

The effect of a weak confinement has been studied numerically by Prasanth *et al.* (2006) in the case where the fluid is allowed to slip at the walls, and by Lazarkov & Revstedt (2008) in the no-slip case. In the latter study, a slight amplitude decrease and a large frequency variation were observed. In a recent work, Sánchez-Sanz & Velazquez (2009) investigated numerically the effect of the confinement by studying the displacement of a square cylinder strongly confined between two parallel walls (ratio between the side of the cylinder and the distance between walls equal to 0.4). Regular oscillations are observed for dense enough cylinders and are accounted for by vortex shedding; below a critical mass, there is a second regime in which the motion is highly irregular with a near-continuum spectrum. No quantitative interpretation of these results was attempted, however.

The present study is focused on a thorough experimental and numerical description and modelling of the instability of a tethered circular cylinder in a strongly confined Hele-Shaw cell geometry and at Reynolds numbers below the vortex shedding threshold. The experimental setup is described in §2 and the numerical procedure in §3. The characteristics of the oscillations, in both the permanent and transient regimes, are discussed in §4. A convenient approach for analysing the onset of the oscillations is to use a simple dynamical model with a small number of parameters: in §5, the force on the cylinder is determined as a function of the transverse position of the cylinder and its derivatives, for forced oscillations. In §6, this expression of the force is used to show that the transverse position of the cylinder satisfies a nonlinear Van der Pol equation when it is free to oscillate. This approach provides a good understanding of the permanent and transient regimes and of the influence of the control parameters (Re and cylinder reduced density ρ_s) on their occurrence. Still, for free oscillations, the domains of observation of the two types of oscillations (CIV and VIV) in the (Re, ρ_s) plane are determined and the variations of their frequency f and amplitude A
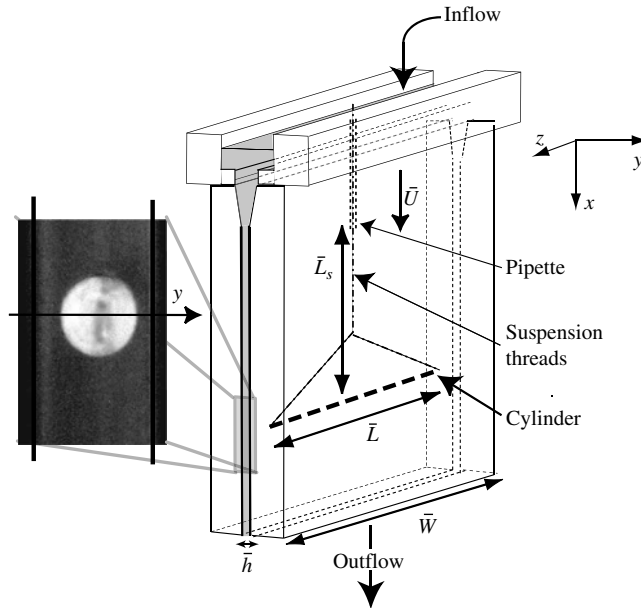
FIGURE 1. Schematic view of the experimental setup.

with Re and ρ_s are discussed. Finally, §7 is devoted to the physical interpretation of the dynamical parameters defined in the Van der Pol model: the coexistence of viscous and inertial effects is found to have a key influence on the onset of the oscillations.

2. Experimental setup

The experimental setup is shown in figure 1: it consists of a Hele-Shaw cell made of two transparent parallel Plexiglas plates, inside which a fluid flows vertically downwards. The lateral sides of the cell are also transparent, allowing for the visualization in the gap of the cell. It has a constant aperture $\bar{h} = 4.9 \pm 0.1$ mm and width $\bar{W} = 90 \pm 0.1$ mm. Note that, in this article, dimensional variables are displayed with an overbar ($\bar{W}, \bar{h}, \ldots$) in contrast with dimensionless ones.

A Plexiglas cylinder of diameter $\bar{D} = 3.2 \pm 0.1$ mm is placed horizontally in the gap. Its density $\bar{\rho}_s = 1190$ kg m^{-3} is close to that of water in order to reduce buoyancy effects (see §4 for a detailed discussion of the gravity effects). In order to minimize the bypass flow at the ends of the cylinder, its length $\bar{L}$ is almost equal to the width of the cell ($\bar{L}/\bar{W} > 0.98$) (see Semin, Hulin & Auradou 2009). The ends of the cylinder are attached by nylon threads of diameter 0.1 mm to a fixed suspension point located close to the inlet (see figure 1). The constant distance between this point and the cylinder is $\bar{L}_s = 150$ mm, i.e. much larger than the aperture $\bar{h}$ of the cell. The cylinder can only translate along the y direction and rotate around the x axis. The influence of the length of the threads has been tested by performing a few experiments with $\bar{L}_s = 65$ mm.

The motion of the cylinder in the aperture of the Hele-Shaw cell is analysed by a Pixelink computer-controlled video camera at a constant frame rate of 22 frames per second (the resolution is 20 pixels mm^{-1}). The displacement of the centre of the cylinder is determined using the method of virtual image correlation (see Semin, François & Auradou 2011). A virtual image of a disc is first created, with a radius
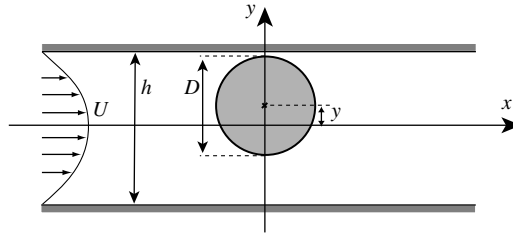
FIGURE 2. Schematic two-dimensional representation of the numerical configuration.

larger than the one of the cylinder in the experimental image and with a grey level varying continuously from 1 (maximal value) at the centre to 0 at its border. The location of the centre of the cylinder is then assumed to correspond to that of the virtual disc when the correlation between the experimental image and the virtual image is optimal. In some experiments, a second video camera was placed on the other lateral side of the cell to verify that the axis of the cylinder remains parallel to the z axis. The absence of rotation around the cylinder axis z has also been verified by observing the motion of defects of the cylinder end.

The fluid is sucked at the bottom of the cell at a constant flow rate by a gear pump (Ismatec MCP-Z) and is then reinjected into the open bath at the top. The flow rate of the pump varies slowly with the counter pressure and can be considered as constant due to the small pressure drop in the present setup; moreover, no oscillation of the level of the free surface of the upper bath is observed. The mean flow is perpendicular to the axis of the cylinder (x direction) and the maximal flow rate is 500 ml min^{-1}. Two fluids are used: water and an aqueous solution containing 1 g l^{-1} of natrosol. The fluids have the same density but different viscosities. The viscosity of water was estimated using a temperature measurement and tabulated values (see Weast & Astle 1982), and is equal to $\bar{\mu} = 0.88 \pm 0.05$ mPa s. A Contraves low shear 30 viscosimeter was used to measure the viscosity and to check the Newtonian nature of the natrosol solution. In the range of shear rates accessible by the rheometer, i.e. 1–100 s^{-1}, the viscosity was found to be constant and equal to $\bar{\mu} = 1.28 \pm 0.05$ mPa s. In order to increase the optical contrast between the fluids and the transparent cylinder, a small amount of dye (nigrosin, 0.1 g l^{-1}) is added to the fluids.

3. Numerical procedure

The velocity and pressure fields as well as the forces on the cylinder were computed by two-dimensional numerical simulations. A schematic view of the numerical configuration is shown in figure 2.

The fluid is modelled using the incompressible Navier–Stokes equations with no-slip boundary conditions on the walls and on the surface of the cylinder (reduced to a disc in these two-dimensional simulations). A parabolic, constant-in-time, Poiseuille velocity profile is imposed at the inlet and a stress-free condition at the outlet. In most simulations, the motion of the cylinder is restricted to a rigid-body translation in the y direction: it is then determined by the component along y of Newton's second law. In a few simulations, threads with a finite length ($\bar{L}_s = 150$ mm) have been modelled in order to evaluate the influence of $\bar{L}_s$: this case will be discussed later.

These equations are solved in a strongly coupled way, using a method similar to the one developed by Janela, Lefebvre & Maury (2005) and Lefebvre (2007).
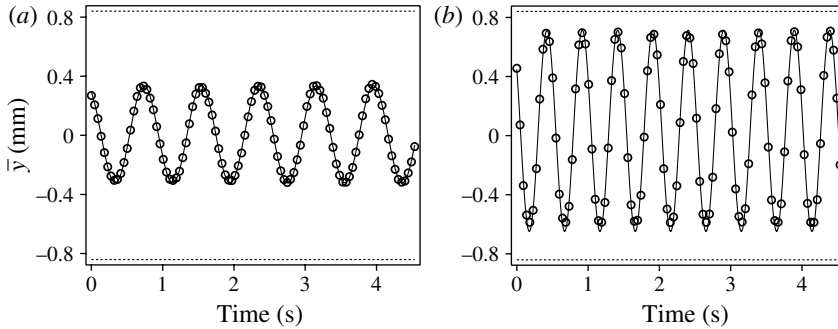
FIGURE 3. Circles: experimental variation of the transverse coordinate $\bar{y}$ of the centre of the cylinder as a function of time for two different Re: (*a*) $Re = 25$ and (*b*) $Re = 50$. Continuous line: fit of the experimental variation by a sine wave. Horizontal dotted lines: maximum possible amplitude of the oscillation (cylinder coming into contact with the walls).

In order to take suitably into account the fluid–cylinder coupling, a single variational form is written on the whole domain, including both the fluid and the cylinder. The constraint due to the rigid motion of the cylinder is handled by penalty, and that due to the suspension threads by duality (the Lagrange multiplier corresponds to the thread tension). In order to deal with the moving rigid domain, the problem is written in an arbitrary Lagrangian–Eulerian formulation (see Hirt, Amsden & Cook 1974). The advection term is treated using a method of characteristics (see Maury 1996), and the variational problem obtained is solved by means of the finite element solver FreeFem++ (see Hecht *et al.* 2010).

The aperture $\bar{h}$, the mean velocity of the fluid $\bar{U}$ and the density of the fluid $\bar{\rho}_f$ are used to define the Reynolds number $Re = \bar{\rho}_f \bar{U} \bar{h}/\bar{\mu}$ and to make the equation and the results dimensionless: the dimensionless diameter D is, for instance, equal to the ratio $\bar{D}/\bar{h}$, and the dimensionless cylinder density ρ_s is the ratio of the density of the cylinder to the density of the fluid. The dimensionless frequency f is defined by $f = \bar{f}\bar{h}/\bar{U}$ and is equal to the Strouhal number of the phenomenon when $\bar{h}$ is used as the characteristic length.

The size of the domain in the direction of the flow ranges from $x = -5h$ to $x = 7h$ and it contains more than 6000 nodes. In order to describe the shape of the cylinder and its evolution in time accurately, the mesh exactly follows the motion of the cylinder along the y direction. Inside the fluid domain, the mesh is subjected to a displacement that satisfies the right boundary conditions and ensures the non-degeneration of mesh cells.

4. Observation and characterization of the instability

Experimentally, when the flow rate is progressively increased from zero, the cylinder remains in a stable position half-way between the walls. Then, for a Reynolds number Re above 20, it starts to oscillate spontaneously in the y direction with its axis remaining parallel to z. Figure 3 displays the experimental variation with time of the location $\bar{y}$ of the axis of the cylinder. The oscillation is regular and stable, and well fitted by the sine function

$$\bar{y}(t) = \bar{A}\sin(2\pi\bar{f}t + \varphi), \tag{4.1}$$
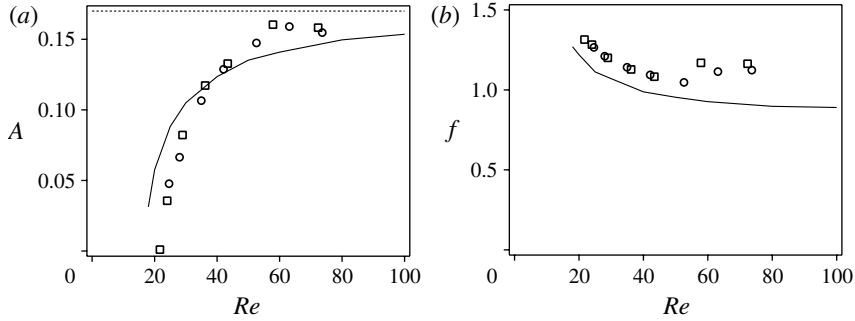
FIGURE 4. Dimensionless amplitude A and frequency f measured experimentally and numerically at $\rho_s = 1.19$: experiments using water ($\circ$); experiments using an aqueous natrosol solution ($\square$); numerical results (solid line); and maximal possible amplitude of the oscillations (dotted line).

where $\bar{A}$ and $\bar{f}$ are the amplitude and frequency of the oscillation (the phase φ takes any value depending on the time origin). Even for Re well above 20 (see figure 3b), the oscillation is still accurately fitted by a sine wave. The same fit is also valid for the numerical results.

An important issue is the influence of the suspension threads. In order to determine this, we first compared the results of experiments performed using threads with the usual length, $\bar{L}_s = 150$ mm, and with a smaller one, $\bar{L}_s = 65$ mm. The measured values of the frequency of the oscillation in the two cases differed by less than 5 % and their amplitude by less than 10 %. As a second test, we compared the results of our usual numerical simulations, in which the cylinder can only translate in the y direction, to those using a more realistic model, including a 150 mm long thread with a fixed upstream end point. The difference between the frequency and amplitude values obtained using these two types of computations is only 6 % at $Re = 20$. In both cases, the influence of the threads decreases when Re increases. These results confirm the minor influence of the suspension threads in the range of Reynolds numbers of interest ($Re > 15$).

Figure 4 displays the variations of the dimensionless amplitude and frequency (or Strouhal number) of the oscillations as a function of Re. The experimental normalized measurement results obtained with the two fluids of different viscosities collapse onto a single curve: this confirms the hypothesis that the Strouhal number depends only on the Reynolds number Re. The numerical threshold and frequency (solid lines in figure 4) also agree within 25 % with the experimental measurements without requiring any adjustable parameter. This difference may be partly accounted for by the three-dimensional effects: the shearing of the thin fluid layer between the lateral wall and the end of the cylinder results in a viscous force on the latter. Drag forces (along y) on the suspension threads may also influence the dynamics of the cylinder. Pendular effects due to gravity and drag on the cylinder only account for a small part of this discrepancy, as discussed in the previous paragraph.

For the density of the cylinder $\rho_s = 1.19$ corresponding to the experiments, the amplitude of the oscillations increases steeply with Re above the threshold and then tends towards a constant value due to the presence of the walls (for other densities, see figure 13). The Strouhal number decreases weakly with Re, which corresponds to a nearly linear increase of the dimensional frequency $\bar{f}$ with the mean flow velocity (or equivalently with the flow rate).
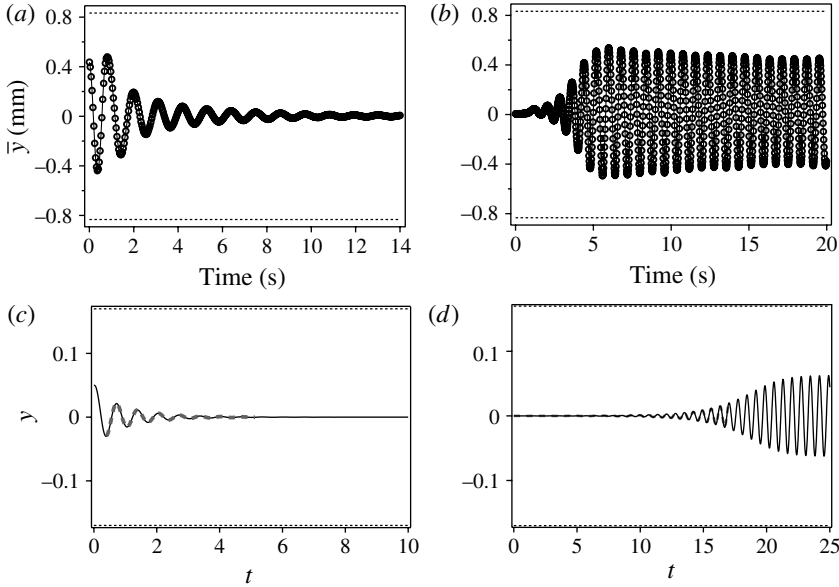
FIGURE 5. Time variation of the displacement y in the transient regime. Experiments: (*a*) Re is reduced from 27 to 17 at $t = 0$; (*b*) Re is increased from 17 to 27 at $t = 0$. Numerical simulations: (*c*) $Re = 14$; (*d*) $Re = 22$. The horizontal dotted lines represent the maximal possible amplitude. The grey dotted lines in (*c*) and (*d*) correspond to a fit with (4.2).

The dynamics of the instability has been investigated by decreasing or increasing the flow rate (and therefore Re) stepwise and studying the subsequent transient regime (see figure 5*a,b*). Equivalent information is obtained from the numerical simulations by assuming that the cylinder is released from an off-centre position at a Reynolds number $Re < Re_c$ (see figure 5*c*) or in the mid-plane of the cell for $Re > Re_c$ (see figure 5*d*).

Below Re_c, damped oscillations of the cylinder are observed and it finally comes to rest half-way between the walls. At a Reynolds number larger than Re_c, the cylinder oscillates spontaneously with an amplitude increasing initially with time before reaching a constant value. In the experiments, there is, in addition, a small (still unexplained) overshoot at the end of the initial phase (see figure 5*b*).

When the amplitude is small (i.e. less than 10 % of the aperture), the variation of y during the initial phase during which the amplitude varies can be fitted by

$$y(t) = A_0 \sin(2\pi f_l t + \varphi) \exp(\xi t), \qquad (4.2)$$

in which f_l and ξ are, respectively, the frequency in the linear regime and the growth rate. The coefficients A_0 and φ depend on the choice of the time origin and have no physical meaning.

The variations of the parameters f_l and ξ as a function of the Reynolds number have been obtained from the numerical simulations described above and are shown in figure 6 (as $\triangledown$ symbols). The frequency f_l is almost independent of Re, while the growth rate increases monotonically with Re from negative to positive values. These different features show that, close to Re_c, the system can be considered as a weakly nonlinear oscillator with a well-defined instability threshold.
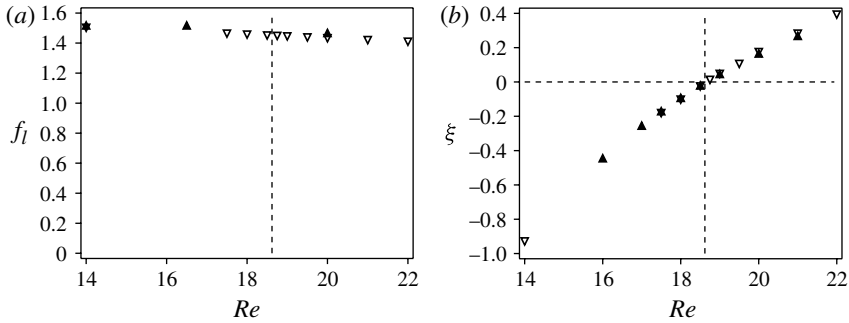
FIGURE 6. Variation of (*a*) the frequency of the transient regime f_l and (*b*) the growth rate ξ of the free oscillations as functions of Re as obtained from numerical simulations: direct simulation of free oscillations ($\triangledown$); values deduced from the characteristics of forced oscillations ($\blacktriangle$). The vertical dashed line shows the resonance frequency. Density of the cylinder $\rho_s = 0.01$.
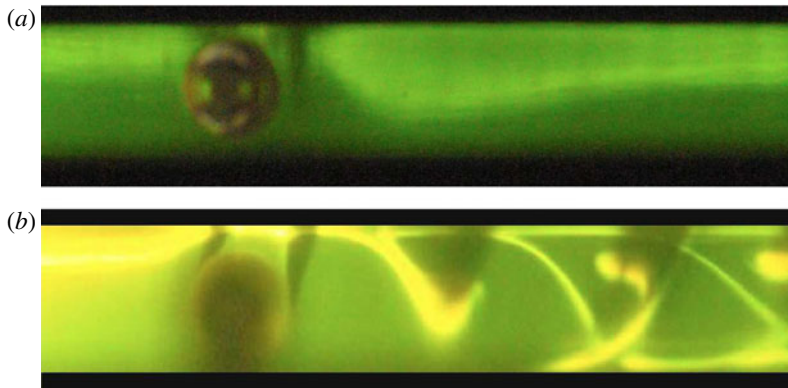
FIGURE 7. (Colour online available at journals.cambridge.org/flm) Comparison of visualizations from (*a*) the side of a fixed cylinder and (*b*) the side of a tethered cylinder free to oscillate, placed in a flow (from left to right in both panels) perpendicular to their axis, with respective Reynolds numbers (*a*) $Re = 60$ and (*b*) $Re = 50$. The axis of the cylinders is perpendicular to the figure and the flow is illuminated by a laser sheet. Fluorescent dye is injected upstream of the cylinder.

The best-known mechanism of flow-induced oscillations in open geometries is the Bénard–Von Kármán vortex shedding instability. The possibility of its occurrence has been tested in the present case by keeping the cylinder at a fixed position and visualizing the flow by means of a fluorescent dye injected in a half-section. In figure 7 by means of such visualizations we compare flows behind a fixed and a free cylinder at similar Reynolds numbers $Re \sim 50$–$60 > Re_c$: no perturbation of the flow is visible behind the fixed cylinder, while distortions of the dye streaks due to the oscillations are clearly visible in the second case.

Actually, for experiments using fixed cylinders, flow oscillations only occur above a threshold Reynolds number $Re_{BVK} = 120 \pm 10$. Numerically, the corresponding threshold is equal to 111, which is similar to the value $Re_{BVK} = 116$ inferred from the interpolation of the numerical data obtained by Chen, Pritchard & Tavener (1995). The confinement therefore significantly increases the threshold of the Bénard–Von
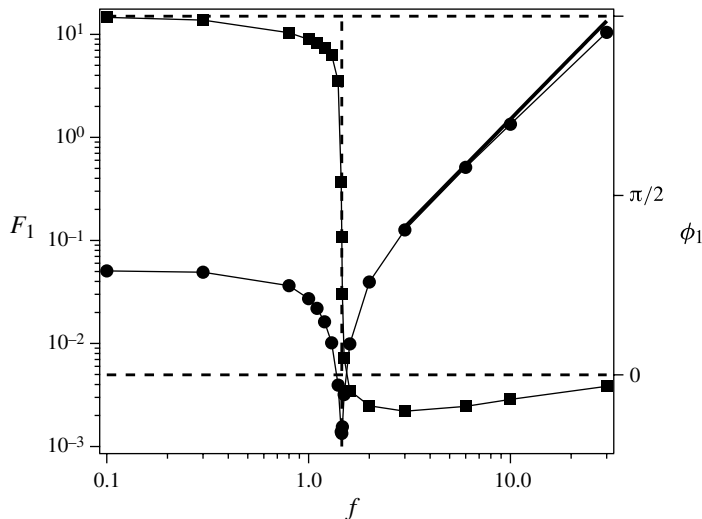
FIGURE 8. Variation of the amplitude F_1 (•) and phase ϕ_1 (■) of the lift force F_y as a function of the frequency f obtained from numerical simulations of the forced oscillations of the cylinder. The slope of the thick straight line is 2. The dashed lines are guides for the eyes (horizontal, values 0 and π of the phase; vertical, resonance frequency). The amplitude of the forced oscillations is $A = 5 \times 10^{-4}$ and $Re = 20$.

Kármán instability compared to the classical value of 47 in open flows; this confirms previous results by, for instance, Shair *et al.* (1963), Zovatto & Pedrizetti (2001) and Rehimi *et al.* (2008). To conclude, Re_{BVK} is much larger than the threshold values $Re_c \sim 20$ measured here; in §§ 6 and 7 we confirm that the instability is not due to vortex shedding.

5. Dynamical system approach in forced oscillations regime

In this section, we use a dynamical system approach to account for these observations. More precisely, we establish a differential equation satisfied by y and depending on a small number of parameters: these are determined by the results of numerical simulations of forced oscillations at different frequencies. This technique has been widely used both experimentally (see e.g. Carberry, Sheridan & Rockwell 2005; Morse & Williamson 2009) and numerically (see e.g. Leontini *et al.* 2006; Placzek, Sigrist & Hamdouni 2009). Practically, the displacement of the centre of the cylinder is forced to vary sinusoidally with time ($y(t) = A \sin(2\pi ft)$) and the simulations allow one to compute the total hydrodynamic lift force $F_y(t)$ on the cylinder (F_y is actually a force per unit length since the simulations are performed in two dimensions). All numerical simulations are performed at the same Reynolds number $Re = 20$ (slightly above the numerical value of Re_c).

5.1. *Force response to a small-amplitude excitation*

We first study the case in which the amplitude A is small enough (5×10^{-4}) to remain in the linear regime. In this case, the lift force F_y also varies sinusoidally, with

$$F_y = F_1 \sin(2\pi ft + \phi_1). \tag{5.1}$$

The phase ϕ_1 is chosen such that $F_1 \geqslant 0$. The variations of the amplitude F_1 and of the phase ϕ_1 of the force F_y as a function of the frequency f are displayed in figure 8.
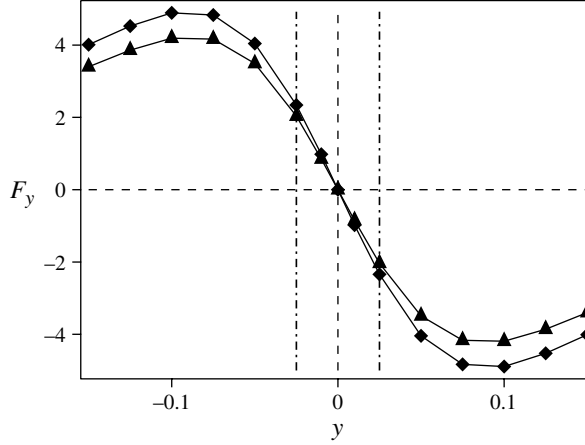
FIGURE 9. Variation of the hydrodynamic force on a fixed cylinder as a function of its position y in the aperture determined from numerical simulations: total force F_y (◆); pressure component of F_y (▲); and approximate limits of the linear regime (vertical dashed-dotted lines). $Re = 20$.

In the low-frequency limit, the instantaneous lift force F_y tends towards that of a fixed cylinder at the same location. The limiting value $\phi_1 = \pi$ of the phase (see left-hand side of figure 8) implies that, for small amplitudes A, F_y is in a direction opposite to the displacement and proportional to it. In this case, the relation between F_y and y may be written as

$$F_y = -ky. \tag{5.2}$$

The parameter k represents the effective stiffness of the system and its value deduced from the numerical simulations is equal to 95. Figure 9 displays the variation of F_y with y obtained from a set of simulations for a fixed cylinder: it confirms the above results and shows that (5.2) is valid up to $y \sim 2 \times 10^{-2}$ (vertical lines). For larger displacements, the modulus of the force levels off and then decreases.

In the opposite high-frequency limit, F_1 is approximately proportional to f^2 (thick solid line in figure 8) while the phase shift ϕ_1 becomes zero. In the linear regime, F_y is therefore proportional to the second derivative of y, i.e. to the transverse acceleration of the cylinder, with

$$F_y = -m_a \ddot{y}. \tag{5.3}$$

The proportionality coefficient m_a in (5.3) represents an added mass associated with the kinetic energy of the fluid; m_a is related to F_1 and A by $F_1 = m_a (2\pi f)^2 A$. Using a regression on the last four high-frequency points in figure 8 leads to $m_a = 0.68$ or equivalently to an additional density $\rho_a = 2.0$.

The mass and stiffness force terms do not induce any net exchange of energy between the flow and the cylinder: the average over one period of the product of either of these terms with $\dot{y}$ (representing the mean power exchanged) is indeed equal to zero. If no other term is present, the phase ϕ_1 can only be equal to 0 or π, which is not in agreement with figure 8: additional dissipative force terms must therefore be introduced. A natural choice is to add a term proportional to the velocity $\dot{y}$. We assume therefore the following expression for the global lift force:

$$F_y = -m_a \ddot{y} - \alpha_0 \dot{y} - ky. \tag{5.4}$$
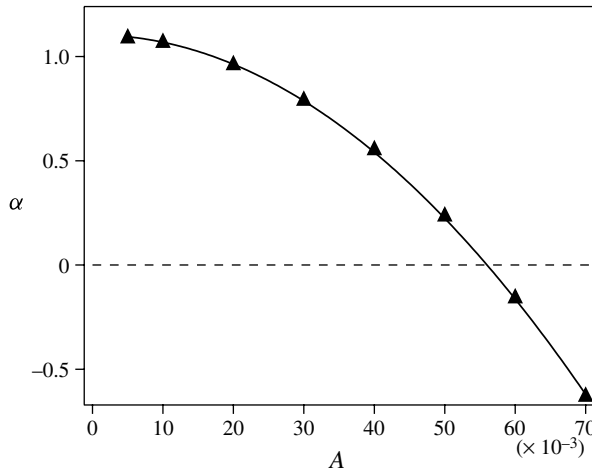
FIGURE 10. Variation of the amplification coefficient α with the amplitude A of a forced oscillation of the cylinder: numerical simulation results ($\blacktriangle$) and parabolic fit (solid line). Oscillation frequency $f = 1.46$ and $Re = 20$.

The coefficient α_0 is determined by equating the expressions of the average energy exchange over one period deduced from (5.4) and (5.1). One obtains

$$\alpha_0 = \frac{F_1}{2\pi fA} \sin(\phi_1), \qquad (5.5)$$

in which F_1 and ϕ_1 are given by the simulations of forced oscillations. The sign of α_0 is therefore the same as that of $\sin(\phi_1)$ and characterizes the stability of the system. For $\alpha_0 > 0$, the energy of the cylinder increases during one period (unstable case), while, for $\alpha_0 < 0$, it loses energy (stable case). In the phase variation curve in figure 8, one sees that $\sin(\phi_1)$ (and therefore α_0) is negative at high frequencies (above $f \sim 1.4$) and positive at lower ones.

5.2. *Force response to a large-amplitude excitation*

As the amplitude A is increased, the response of the lift force becomes nonlinear and (5.4) is no longer valid. In order to analyse its variation with time, the force is decomposed into a Fourier series,

$$F_y(t) = \sum_{q=1}^{\infty} F_q \sin(2\pi qft + \phi_q), \qquad (5.6)$$

in which the phases ϕ_q are chosen so that $F_q \geqslant 0$.

As for the linear regime, the coefficient α generalizing α_0 is estimated numerically by computing the average power transferred to the cylinder over one period. Using the decomposition of F_y into a Fourier series leads to $\alpha = (F_1/2A\pi f) \sin(\phi_1)$. The variation of α with A, determined by numerical simulations for a fixed frequency, is displayed in figure 10 and is well fitted by

$$\alpha = \alpha_0 - (\beta/4)A^2, \qquad (5.7)$$

in which α_0 is the value in the low-amplitude regime. The force term $\alpha_0 \dot{y}$ of (5.4) then becomes, still for sine-wave forced oscillations,

$$F_y = (\alpha_0 - \beta y^2)\dot{y}. \tag{5.8}$$

At different frequencies, the variation of α with respect to the amplitude A is similar: in all cases, the coefficient characterizing the gain of energy decreases with the amplitude up to a critical value above which energy must be input externally to keep A constant.

As the amplitude A increases, the stiffness k also varies. Figure 9 shows that, outside the linear domain sketched by the two vertical dotted lines, the effective stiffness k decreases with A. However, this variation is small enough to change the dynamics of the cylinder quantitatively but not qualitatively. We verify in the following sections that the characteristics of the oscillation are well approximated by assuming a constant stiffness k in the following sections.

6. Free oscillations

6.1. *Equation of motion of a free cylinder and Van der Pol oscillator*

For a free cylinder, the global hydrodynamic force F_y on the cylinder is related to its acceleration $\ddot{y}$ by Newton's second law:

$$m_s \ddot{y} = F_y. \tag{6.1}$$

Moreover, the relations (5.4) and (5.8) between F_y and the displacement y and its time derivatives remain valid. Equation (6.1) then becomes

$$(m_a + m_s)\ddot{y} - (\alpha_0 - \beta\,(y)^2)\dot{y} + ky = 0, \tag{6.2}$$

which shows that the transverse position y of the cylinder satisfies the classical Van der Pol equation (see e.g. Nayfeh & Mook 1995; Manneville 2004). Close to the threshold, the oscillation is quasi-sinusoidal. The frequency f_l and the growth rate ξ of the oscillations predicted by (6.2) are then related to its parameters by

$$f_l = \frac{1}{2\pi}\sqrt{\frac{k}{m_a + m_s}} \tag{6.3}$$

and

$$\xi = \frac{\alpha_0}{2(m_a + m_s)}. \tag{6.4}$$

Note that, owing to the influence of the mass m_s of the cylinder, the frequency f_l of the free oscillations is lower than the resonance frequency $f_r = \sqrt{(k/m)}/(2\pi)$ for forced oscillations and decreases with m_s.

The frequency f_l and the growth rate ξ can then be predicted by using in (6.3) and (6.4) the values of k, m_a and α_0 deduced in §5 from the simulations of forced oscillations. These values are compared in figure 6(a,b) to those obtained from direct simulations of free oscillations in transient regimes (see figure 5c–d). The two sets of values are in good agreement without requiring any adjustable parameter; this confirms the validity of the above description.

In the Van der Pol equation, the sign of α_0 determines whether the system tends towards a fixed point or a limit cycle in the permanent regime: if $\alpha_0 < 0$, the
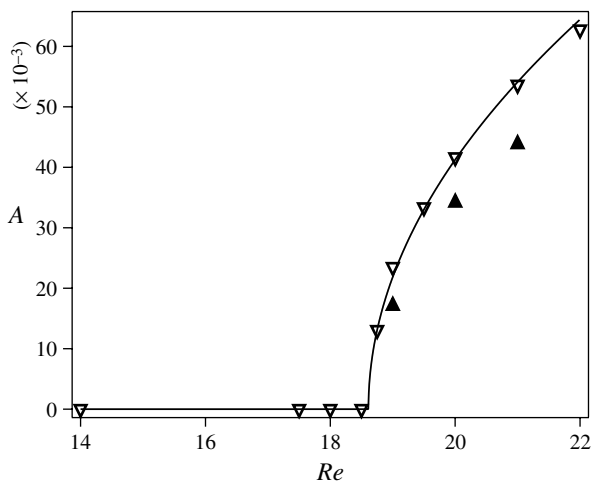
FIGURE 11. Amplitude of the free oscillations in the stationary regime as a function of Re for $\rho_s = 0.01$: numerical simulation results for free oscillations ($\bigtriangledown$); predictions of (6.5) from the Van der Pol equation ($\blacktriangle$); and fit by a square-root variation (solid line).

cylinder remains motionless half-way between the walls, and if $\alpha_0 > 0$, it oscillates spontaneously. In this latter case, the amplitude A of the oscillation is then limited by the nonlinear term $-\beta (y)^2 \dot{y}$ of (6.2). In the quasi-sinusoidal stationary regime, A is given by

$$A = 2\sqrt{\alpha_0/\beta}. \tag{6.5}$$

Like f_l and ξ, the amplitude may therefore be computed by using in (6.5) values of α_0 and β obtained from numerical simulations of forced oscillations. In the same range of Reynolds numbers as above, these values have a similar variation as those corresponding to free oscillations (figure 11). Above the threshold, the variation of A is well fitted by a variation proportional to $\sqrt{Re - Re_c}$.

Overall, the free oscillations of the cylinders display several clear-cut features: weak variation of the frequency near Re_c, continuous increase of ξ from negative values below Re_c to positive ones above, and amplitude increasing as $\sqrt{Re - Re_c}$. These features are all characteristic of a supercritical Hopf bifurcation, which is the usual one for a system described by a Van der Pol equation.

The expressions of the frequency, growth rate and amplitude given above are only valid in the quasi-sinusoidal regime. It is possible to verify that the oscillations are quasi-sinusoidal directly from the Van der Pol equation, by computing the quality factor $Q = 2\pi f_r m_a/\alpha_0$. Near the threshold, the quality factor is very high ($Q = 23$ at $Re = 20$) as expected and the oscillation is quasi-sinusoidal at the frequency f_l in both the transient and permanent regimes. For Re farther from the threshold, the quality factor decreases ($Q = 2.4$ at $Re = 30$) but remains large enough to obtain quasi-sinusoidal oscillations.

It must finally be pointed out that the Van der Pol equation involves directly the transverse displacement y from equilibrium and its first and second time derivatives instead of a typical velocity of the wake as e.g. in the study of vortex-induced vibrations by Facchinetti, de Langre & Biolley (2004).
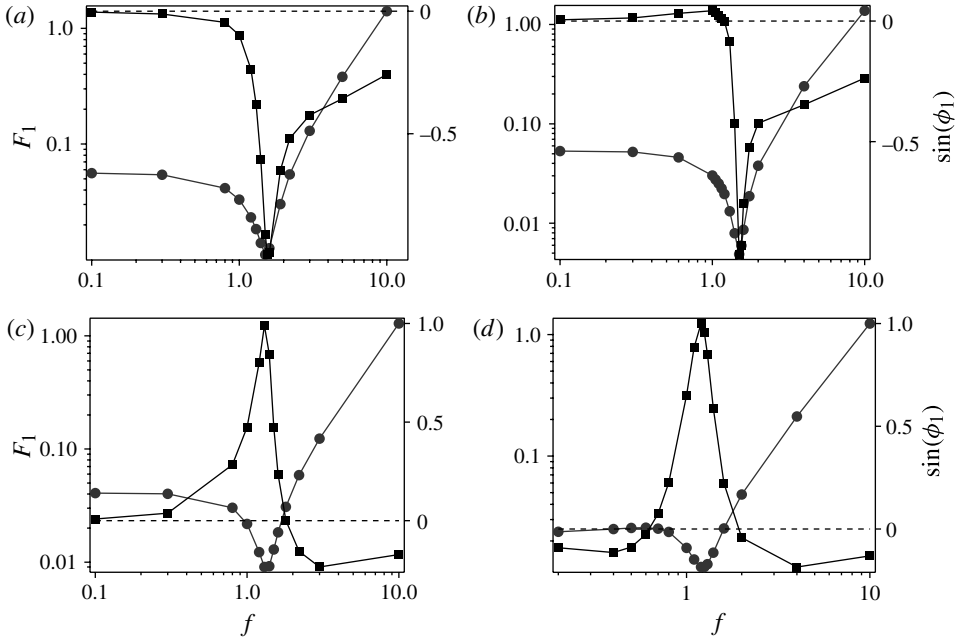
FIGURE 12. Variation of the amplitude F_1 ($\bullet$) and the sine of the phase ϕ_1 ($\blacksquare$) of the hydrodynamic force as a function of the forced oscillation frequency f at different Reynolds numbers Re: (*a*) $Re = 14$, (*b*) $Re = 16.5$, (*c*) $Re = 30$ and (*d*) $Re = 50$. Amplitude $A = 5 \times 10^{-4}$.

6.2. *Influence of the mass of the cylinder on the stability of the free oscillation*

As mentioned above, a free cylinder oscillates spontaneously at the frequency $f_l = \sqrt{k/(m_a + m_s)}/(2\pi)$ only if $\alpha_0 > 0$ (or equivalently $\sin(\phi_1) > 0$). The range of values of Re for which this condition is satisfied and its dependence on m_s (or equivalently ρ_s) may be inferred from figure 12, representing $\sin(\phi_1)$ as a function of frequency at different Reynolds numbers.

For $Re = 14$ (figure 12*a*), $\sin(\phi_1)$ is always negative even if the frequency f_l is shifted towards lower values by increasing the mass m_s: the cylinder therefore remains at rest regardless of m_s.

For $Re = 16.5$ (figure 12*b*), one still has $\sin(\phi_1) < 0$ at f_r, and thus a massless cylinder does not oscillate. However, when f_l is reduced by increasing m_s, $\sin(\phi_1)$ becomes positive and the oscillations appear. This means that the increased inertia of denser cylinders reduces the threshold Reynolds number Re_c.

Increasing again Re to 20 (figure 8) or 30 (figure 12*c*), $\sin(\phi_1)$ is positive at all frequencies lower than f_r: the cylinder oscillates regardless of its density.

For $Re = 50$ (figure 12*d*), $\sin(\phi_1)$ is positive for $f = f_r$ and negative at low frequencies. In contrast with case (*b*), dense cylinders remain stable while the massless one oscillates.

6.3. *Free oscillation regime map as a function of ρ_s and Re*

In view of the above results, a systematic study of the variations of the amplitude and frequency of the oscillations has been performed over a broad range of values of Re ($0 < Re < 130$) and of relative density ρ_s ($0 < \rho_s < 15$). The results are plotted in figure 13(*a,b*).
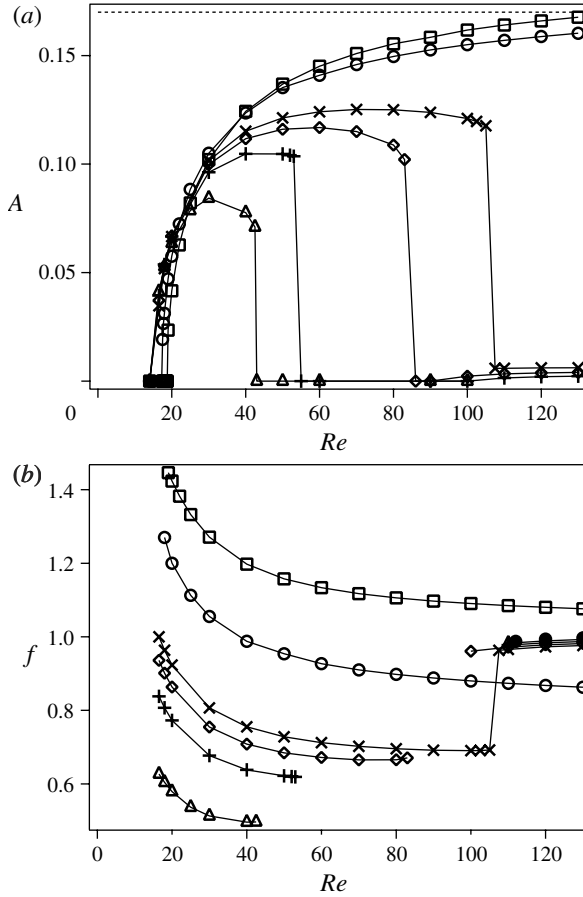
FIGURE 13. Influence of the mass of the cylinder on the variation of (*a*) the amplitude and (*b*) the frequency (only defined if the amplitude is not vanishing) of the free oscillations as a function of *Re* (from numerical simulations): $\rho_s = 0.01$ ($\square$); $\rho_s = 1.19$ ($\circ$); $\rho_s = 4$ ($\times$); $\rho_s = 5$ ($\diamond$); $\rho_s = 7$ ($+$); and $\rho_s = 15$ ($\triangle$). The dashed horizontal line represents the maximum possible amplitude. Also shown is the frequency of the instability of the flow downstream of a fixed cylinder ($\bullet$).

At all values of the density ρ_s investigated, the CIV appear at a low critical Reynolds number Re_c decreasing slowly from 19 to 15 as ρ_s varies from 0 to 15. Right above the threshold Re_c, the frequency f decreases with Re and then becomes almost constant. As could be expected from (6.3), the frequency f at the threshold increases at low values of ρ_s. The amplitude rises as $\sqrt{Re - Re_c}$ right above the threshold in a similar way for all densities.

Consistently with the results of §6.2, for large densities ρ_s (symbols $\triangle$, $+$ and $\diamond$), CIV disappear above a value of Re decreasing as ρ_s increases. If Re is increased further, the cylinder oscillates again slightly below the critical value Re_{BVK} corresponding to the appearance of vortex shedding ($Re_{BVK} \sim 111$ for this geometry). The amplitude of the latter oscillations is very small ($A < 0.01$), and the frequency is almost independent of the density and equal to the frequency of the vortex shedding behind a fixed cylinder. This indicates that these oscillations are not of the CIV type but are due to vortex shedding.
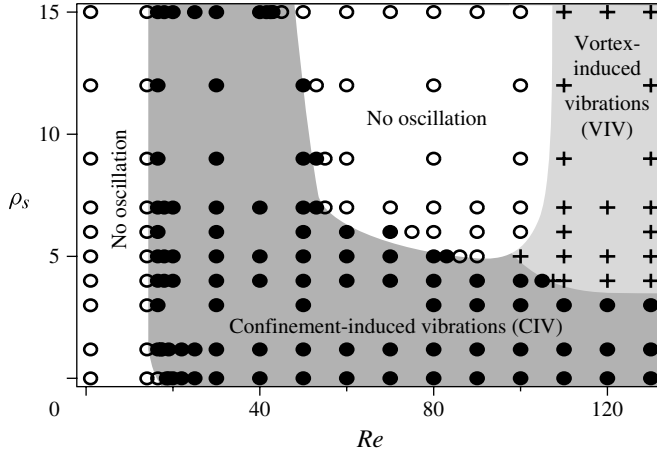
FIGURE 14. Phase diagram of the behaviour of the cylinder for different *Re* and ρ_s as obtained from numerical simulations: cylinder stable in the midplane of the walls (○); CIV oscillations (●); VIV oscillations (+). The grey shades are qualitative guides for the eye.

For small densities, i.e. approximately for $\rho_s < 4$, the variations of both *A* and *f* with *Re* are continuous. No feature of the corresponding curves in either figure 13(*a*) or 13(*b*) suggests an influence of vortex shedding; for example, *f* differs from the frequency behind a fixed cylinder. For such values of ρ_s, we conclude that the CIV mechanism is dominant even at Reynolds numbers high enough for the occurrence of VIV.

The phase diagram of figure 14 displays the different behaviours of the cylinder observed as a function of *Re* and ρ_s. For densities $\rho_s > 4$, CIV and VIV were observed in distinct domains: these are separated by a region of width ΔRe increasing with ρ_s and inside which there are no oscillations. For $\rho_s < 4$, only CIV occurred. For $\rho_s = 4$, the oscillations shifted abruptly from the CIV to the VIV regime as *Re* increased.

7. Hydrodynamic interpretation of the dynamical parameters of the instability

Equation (6.2) accounts well for the growth (or decay) of the oscillations with time and for the relation between measurements on forced and free oscillations. However, this global dynamical system approach does not provide information on the physics of the flow at the local scale. In this section, we investigate the relation between the coefficients of the equation and the characteristics of the flow field.

7.1. *Origin of the stiffness coefficient*

The stiffness coefficient – defined by (5.2) – characterizes the restoring force exerted on a fixed cylinder away from the centre of the Hele-Shaw cell. As seen in figure 9, the total force F_y is mainly due to the pressure component: its value can be interpreted from the pressure field displayed in figure 15 for *Re* = 20. The pressure variation is particularly important in the region separating the cylinder and the walls, referred to as *channels* in the following.

For *Re* = 1, there is a fore–aft symmetry of both the velocity and the pressure gradient (see figure 15*a,b*) because the viscous effects are dominant. Owing to this symmetry, the lift force F_y vanishes (almost), regardless of the position of the cylinder in the gap. This is no longer the case for *Re* = 20 (see figure 15*c,d*). In that case, the
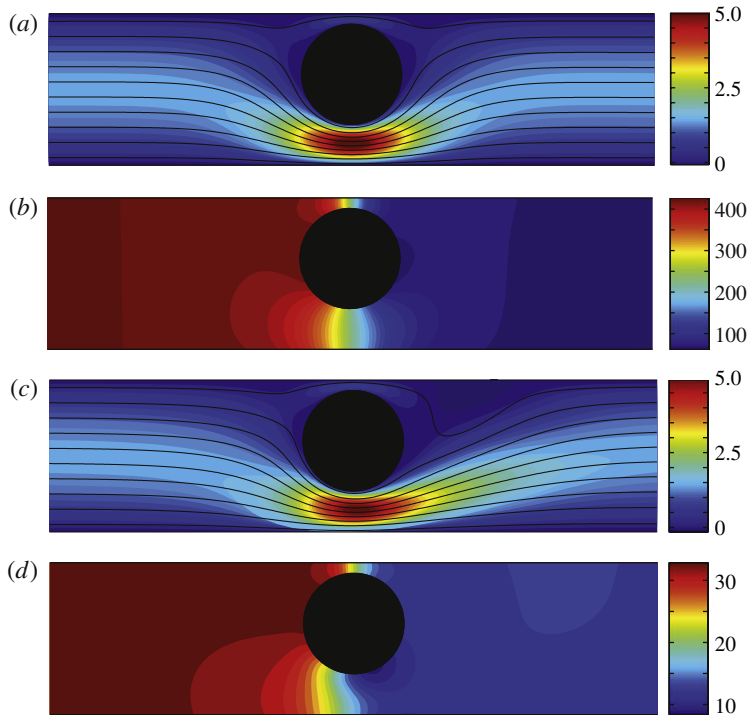
FIGURE 15. (Colour online) Numerical simulation of the flow (from left to right) around a fixed cylinder at (*a,b*) *Re* = 1 and (*c,d*) *Re* = 20. In (*a*) and (*c*) the colour bar (greyscale) represents the velocity component v_x; and full lines are streamlines. In (*b*) and (*d*) the colour bar (greyscale) represents the pressure field.

pressure on the surface of the cylinder is higher in the upper (narrower) channel than in the lower (larger) channel, for all values of *x* (between $-D/2$ and $D/2$). As a result, the global resultant force is non-zero and oriented downwards: it acts as a restoring force, in agreement with figure 9.

Because the pressure is almost uniform upstream and downstream of the cylinder, the higher pressure at a given *x* in the upper (narrower) channel can be explained by the fact that the pressure gradient is more symmetrical about the axis $x = 0$ in this latter channel. The asymmetry along *y* in a channel is indeed due to inertial effects, and is more pronounced when *Re* increases. The local *Re* is significantly higher in the lower (larger) channel than in the upper (narrower) one due to larger local width and velocity, which explains the observed pressure field at *Re* = 20.

At lower values of the dimensionless diameter *D*, the result might have been different as shown by Zovatto & Pedrizetti (2001) for *D* = 0.2. In this case, a contribution to the force due to the curvature of the velocity profile leads to two symmetrical additional equilibrium positions that are not in the mid-plane between the walls.

7.2. *Added mass*

Forces proportional to the acceleration of a solid body in a fluid are classical in fluid dynamics. Such forces are partly due to the acceleration of the fluid, and are thus observed even in irrotational flows. For an irrotational fluid without base flow,
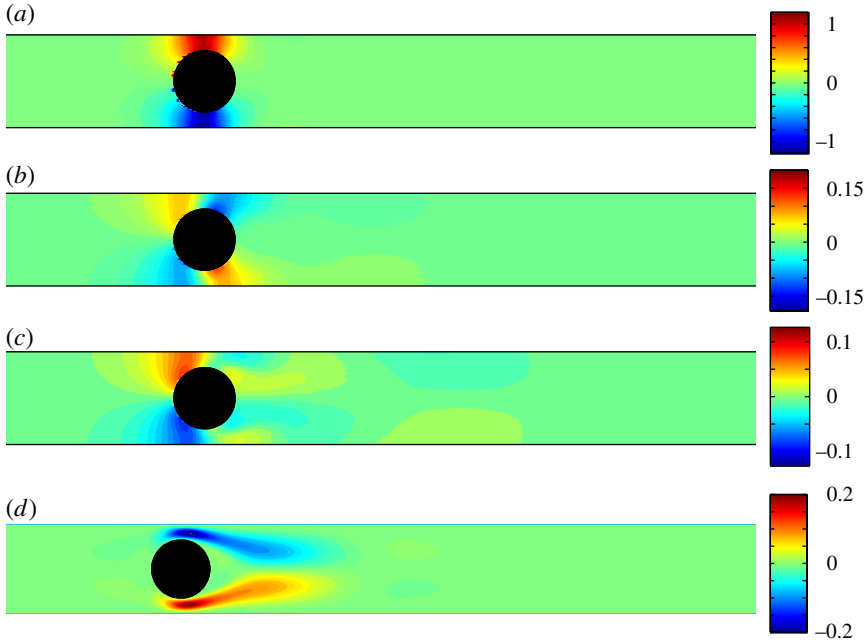
FIGURE 16. (Colour online) Maps of the pressure perturbation $\delta p(x, y)$ induced by an upwards motion of the cylinder at a velocity $\dot{y} = 0.013$, as a function of Re (from numerical simulations of forced oscillations at $f = 0.2$): (*a*) $Re = 1$, (*b*) $Re = 20$, (*c*) $Re = 50$, and (*d*) Bernoulli's pressure difference term for $Re = 20$.

the additional density can be estimated numerically, and is equal to $\rho_a = 1.44$ at $y = 0$. This is lower than the values $\rho_a = 3$ calculated from the stiffness and the resonance frequency. It also differs from the value $\rho_a = 2$ deduced from the forced oscillations at $f = 10$, using $m_a = F_1/(A\,(2\pi f)^2)$. These differences may be due to the relatively low value of Re or to the influence of the base flow. Other authors have also reported values of the added mass differing from the potential case for vortex-induced vibrations (see Williamson & Govardhan 2004).

7.3. *Destabilizing force term*

Here, we analyse the origin of the term $\alpha_0 \dot{y}$ by considering the variations of pressure $\delta p(x, y) = p(x, y) - p_0(x, y)$ between the case of a forced oscillation, $p(x, y)$, and that of a static cylinder, $p_0(x, y)$. The frequency $f = 0.2$ is low enough that the influence of the added mass is negligible; the pressure field corresponds to a transverse location $y = 0$ of the cylinder at which the stiffness term ky becomes zero. Figure 16(*a–c*) display the pressure perturbations corresponding to three different Reynolds numbers (the force F_y on a fixed cylinder at $y = 0$ vanishes due to the symmetry, and the use of the perturbation of the pressure δp instead of the pressure p is justified by the clarity of the figure).

At the lowest Reynolds number $Re = 1$ (figure 16*a*), δp is positive above the cylinder and negative below it: the orientation of the resultant force is therefore opposite to the cylinder velocity so that α_0 is negative and the system is stable. In this case, owing to the linearity of the Stokes equation, the force is equal to the Stokes drag on a cylinder moving in a fluid at rest, which always opposes the motion.

For $Re = 20$ (figure 16b), two additional lobes appear downstream of the cylinder: their signs are opposite to that of the previous ones and the magnitude of the corresponding pressure variation is larger: the resultant force is then in the same direction as the cylinder velocity. In this case, α_0 is positive (for $f = 0.2$) and the oscillation is amplified (at least if $f_l = f$).

For $Re = 50$ (figure 16c), the downstream lobes disappear while the upstream ones are still present. The pressure is therefore again higher above the cylinder than below, leading to a resultant force in the direction opposite to the cylinder velocity. As a result, $\alpha_0 < 0$ (for $f = 0.2$) and the cylinder is again stable if $f_l = f$, which corresponds to a cylinder of large mass. The reduction of the downstream lobes may be due to the recirculation zone present behind the cylinder in the base flow.

These results show that the pressure distribution strongly depends on the Reynolds number and, therefore, on the influence of inertia. As a first approach, we tried to estimate its effect by the Bernoulli pressure theorem, leading to $\delta p_B \sim -V_b \cdot v$, in which V_b and v are the velocities for the base and the perturbed flows, respectively (this is only a rough approximation because of the influence of viscous forces, in contrast with the assumptions of the theorem). Low- and high-pressure regions of the same sign as in the downstream lobes for $Re = 20$ indeed appear. However, no upstream lobes are observed and, moreover, this effect should be stronger for $Re = 50$ instead of disappearing. More refined models taking into account viscous forces are therefore needed.

We notice that the interpretation of the destabilizing term, like that of the effective stiffness and the added mass, does not involve vortex shedding.

8. Conclusion

Using experiments and numerical simulations, we have demonstrated the existence and studied the characteristics of a novel hydrodynamic instability for a tethered cylinder perpendicular to a flow in a Hele-Shaw cell. We showed that the confinement of the cylinder is essential to this instability, which we called CIV.

These CIV differ significantly from VIV induced by vortex shedding at the rear of the cylinder. The CIV appear indeed at a Re value much lower than the threshold for VIV (15–20 instead of 111). Their amplitude increases sharply above the threshold, and their frequency decreases with ρ_s. In contrast, VIV are characterized in our configuration by small amplitudes and a frequency almost constant with ρ_s. For densities of the cylinders ρ_s smaller than approximately 4, the oscillations remain in the CIV mode up to the largest values of Re investigated. For higher densities $\rho_s > 4$, an oscillation-free regime exists between the CIV at low Re and the VIV at higher ones.

Close to the threshold for the CIV, the transverse position of the cylinder satisfies a Van der Pol equation. This equation characterizes conveniently the dynamics of the system by a small number of physically meaningful parameters, which were determined in the forced oscillation mode: a stiffness, a mass and a destabilizing term. The stiffness term has a purely hydrodynamic origin and results from the confinement of the flow. The mass term includes the mass of the cylinder, which may be equal to zero without suppressing the oscillations, and the added hydrodynamic mass. The frequency can be calculated using the stiffness and the total mass, which provides an interpretation of the variation of the frequency with ρ_s. The third term is proportional to the velocity and determines the stability of the system. It results from tiny variations of the local pressure distribution in the region between the cylinder and the walls

and involves a subtle balance between viscous and inertial effects, which cannot be explained by Bernoulli's theorem. The Van der Pol model describes the onset of the CIV as a supercritical Hopf bifurcation in agreement with the observations for the free oscillations.

Different questions remain open regarding these effects, which may lead to various applications such as mixers or low-speed flow meters. The onset of the CIV has been studied here in detail but their disappearance and the transition towards VIV are also important issues as well as the possible coexistence of the CIV and VIV regimes at low cylinder densities and high *Re*. The present study has only investigated CIV for one value of the ratio of the cylinder diameter to the cell aperture. The variation of the characteristics of the oscillations as a function of this ratio will have to be investigated in order to quantify the influence of confinement.

Acknowledgements

REFERENCES

ANAGNOSTOPOULOS, P. & BEARMAN, P. W. 1992 Response characteristics of a vortex-excited cylinder at low Reynolds number. *J. Fluids Struct.* **6**, 39–50.

CARBERRY, J., SHERIDAN, J. & ROCKWELL, D. 2005 Controlled oscillations of a cylinder: forces and wake modes. *J. Fluid Mech.* **538**, 31–69.

CHEN, J.-H., PRITCHARD, W. G. & TAVENER, S. J. 1995 Bifurcation for flow past a cylinder between parallel plates. *J. Fluid Mech.* **284**, 23–41.

COSSU, C. & MORINO, L. 2000 On the instability of a spring-mounted circular cylinder in a viscous flow at low Reynolds numbers. *J. Fluids Struct.* **14**, 183–196.

FACCHINETTI, M. L., DE LANGRE, E. & BIOLLEY, F. 2004 Coupling of structure and wake oscillators in vortex induced vibrations. *J. Fluids Struct.* **19**, 123–140.

GABBAI, R. D. & BENAROYA, H. 2005 An overview of modelling and experiments of vortex-induced vibration of circular cylinders. *J. Sound Vib.* **282**, 575–616.

GOVARDHAN, R. & WILLIAMSON, C. H. K. 2002 Resonance forever: existence of a critical mass and an infinite regime of resonance in vortex-induced vibration. *J. Fluid Mech.* **473**, 147–166.

HECHT, F., PIRONNEAU, O., LE HYARIC, A. & OHTSUKA, K. 2010 FreeFem++ manual. http://www.freefem.org/ff++/.

HIRT, C. W., AMSDEN, A. A. & COOK, J. L. 1974 An arbitrary Lagrangian–Eulerian computing method for all flow speeds. *J. Comput. Phys.* **14**, 227–253.

HOROWITZ, M. & WILLIAMSON, C. H. K. 2006 Dynamics of a rising and falling cylinder. *J. Fluids Struct.* **22**, 837–843.

JANELA, J., LEFEBVRE, A. & MAURY, B. 2005 A penalty method for the simulation of fluid–rigid body interaction. *ESAIM: Proc.* **14**, 115–123.

LAZARKOV, M. & REVSTEDT, J. 2008 Flow-induced motion of a short circular cylinder spanning a rectangular channel. *J. Fluids Struct.* **24**, 449–466.

LEFEBVRE, A. 2007 Fluid–particle simulations with Freefem++. *ESAIM: Proc.* **18**, 120–132.

LEONTINI, J. S., STEWART, B. E., THOMPSON, M. C. & KOURIGAN, K. 2006 Wake state and energy transitions of an oscillating cylinder at low Reynolds number. *Phys. Fluids* **18**, 067101.

MANNEVILLE, P. 2004 *Instabilities, Chaos and Turbulence: an Introduction to Nonlinear Dynamics and Complex Systems*. Imperial College Press.

MAURY, B. 1996 Characteristics ALE method for the unsteady 3D Navier–Stokes equations with a free surface. *Comput. Fluid Dyn.* **6**, 175–188.

MEIS, M., VARAS, F., VELÀSQUEZ, A. & VEGA, J. M. 2010 Heat transfer enhancement in micro-channels caused by vortex promoters. *Intl J. Heat Mass Transfer* **53**, 29–40.

MITTAL, S. & SINGH, S. 2005 Vortex-induced vibrations at subcritical *Re*. *J. Fluid Mech.* **534**, 185–194.

MORSE, T. L. & WILLIAMSON, C. H. K. 2009 Prediction of vortex-induced vibration response by employing controlled motion. *J. Fluid Mech.* **634**, 5–39.

NAYFEH, A. H. & MOOK, D. T. 1995 *Nonlinear Oscillations*. John Wiley.

PLACZEK, A., SIGRIST, J.-P. & HAMDOUNI, A. 2009 Numerical simulation of an oscillating cylinder in a cross-flow at low Reynolds number: forced and free oscillations. *Comput. Fluids* **38**, 80–100.

PRASANTH, T. K., BEHARA, S., SINGH, S. P. & MITTAL, S. 2006 Effect of blockage on vortex-induced vibrations at low Reynolds numbers. *J. Fluids Struct.* **22**, 865–876.

REHIMI, F., ALAOUI, F., NASRALLAH, S. B., DOUBLIEZ, L. & LEGRAND, J. 2008 Experimental investigation of a confined flow downstream of a circular cylinder centred between two parallel walls. *J. Fluids Struct.* **24**, 855–882.

SÁNCHEZ-SANZ, M., FERNANDEZ, B. & VELAZQUEZ, A. 2009 Energy-harvesting microresonator based on the forces generated by the Kármán street around a rectangular prism. *J. Microelectromech. Syst.* **18**, 449–457.

SÁNCHEZ-SANZ, M. & VELAZQUEZ, A. 2009 Vortex-induced vibration of a prism in internal flow. *J. Fluid Mech.* **641**, 431–440.

SARPKAYA, T. 2004 A critical review of the intrinsic nature of vortex-induced vibrations. *J. Fluids Struct.* **19**, 389–447.

SEMIN, B., FRANÇOIS, M. L. M. & AURADOU, H. 2011 Accurate measurement of curvilinear shapes by virtual image correlation. *Eur. Phys. J. Appl. Phys.* **56**, 10701.

SEMIN, B., HULIN, J. P. & AURADOU, H. 2009 Influence of flow confinement on the drag force on a static cylinder. *Phys. Fluids* **21** (10), 103604.

SHAIR, F. H., GROVE, A. S., PETERSEN, E. E. & ACRIVOS, A. 1963 The effect of confining walls on the stability of the steady wake behind a circular cylinder. *J. Fluid Mech.* **17**, 546–550.

SHIELS, D., LEONARD, A. & ROSHKO, A. 2001 Flow-induced vibration of a circular cylinder at limiting structural parameters. *J. Fluids Struct.* **15**, 3–21.

WEAST, R. C. & ASTLE, M. J. 1982 *Handbook of Chemistry and Physics*. CRC.

WILLIAMSON, C. H. K. & GOVARDHAN, R. 2004 Vortex-induced vibrations. *Annu. Rev. Fluid Mech.* **36**, 413–455.

WILLIAMSON, C. H. K. & GOVARDHAN, R. 2008 A brief review of recent results in vortex-induced vibrations. *J. Wind Engng Ind. Aerodyn.* **96**, 713–735.

ZOVATTO, L. & PEDRIZETTI, G. 2001 Flow about a circular cylinder between parallel walls. *J. Fluid Mech.* **440**, 1305–1320.